„Handbook on Biofunctional Surfaces“, Pan Stanford Publishing in Singapore, W. Knoll (ed.), (2013), pages 139-187

MO-CVD on Patterned SAMs*

Silvia Mittler
Department of Physics and Astronomy, The University of University of Western Ontario, London, Ontario N6A 3K7, Canada
smittler@uwo.ca

This article gives an overview on organo-metallic chemical vapor deposited (OMCVD) metal layers and metal nanoparticles (NP) on self-assembled monolayers (SAMs), which have been laterally patterned. Both enabling /disabling as well as growth and non-growth resist patterning in SAMs will be mentioned.
Simple methods like stamping of lateral SAM structures with an PDMS (polydimethylsiloxane) stamp or more complex pattering technologies like focused ion beam (FIB) nanolithography will be discussed.
Copper, palladium, platinum, gold, gallium nitride and mercury are the metals/materials of interest, whereas the focus of this chapter lies on AuNPs, due to their promising application in biosensing. Nobel metal NPs show an interesting resonant absorption feature called the localized surface plasmon resonance (LSPR). This LSPR exhibits an absorption band in the visible and its spectral position is extremely sensitive to environmental changes of the NP: both with respect to the refractive index of surrounding materials as well as with respect to a colloidal or clustered NP architectures.

1.1 INTRODUCTION

The adsorption of organosulfur compounds like thiols, sulfides, and disulfides on the surfaces of coinage metals (i.e., Cu, Ag, and Au) to fabricate so called self-assembled monmolayers (SAMs) represents a chemisorption system with unique and interesting properties, [1-4]. While the initial steps of the self-assembly process, including aspects of substrate characteristics [5,6], and the structural properties of the resulting SAMs, are still matters of intense research effort, the focus of much activity is the deposition of further layers onto the SAMs. Both inorganic [7-14] organic [15-17] materials and living cells, such as bacteria [18] are under consideration. Here we focus on SAMs carrying a thiol moiety as the functional head group to allow coinage metal immobilization.
Two immobilization schemes are considered: a) metal surfaces carrying a dithiol SAM and b) oxidic surfaces (glass or oxidized silicon wavers) with an SH-terminated silane SAM. These SH-modified surfaces allow the attachment of metallic ions [7,8], metals (e.g., by conventional vacuum deposition technologies or electrochemical reduction of metallic ions in solution) [9-14] and as well as the deposition of presynthesized Au nanoparticles (NPs) [19-24].
CVD is an alternative and commonly used technique for growing thin films of a variety of materials for a broad range of applications, [25].
However, CVD is commonly known for the need of rather high operation temperature, typically well above 200 °C. At these temperatures most organic materials will suffer in a form of destruction or at least chemical alteration.
Afford has been put into the coating of prefabricated nanoobjects with thin films of silica, carbon or gold by CVD methods, [26-28]. Some work has been performed on growing AuNPs and nanorods via precursor assisted CVD, e.g. with aerosol assisted CVD using hydrogen tetrachloroaurate(III) [29] or in the channel of mesoporous silica with dimethyl(hexafluoro-acetylacetoato)gold(III), [30].
Since recent years CVD of materials is also carried out on top of SAMs. This is due to the availability of organometallic (OM) precursors allowing CVD processes under mild thermal activation (T ~ 200°C for silanes, and 60-70 °C for thiols), which is compatible with most organic materials, critical with a SAM on a gold or silver, and to some extend

* OMCVD: organometallic chemical vapor deposition, SAM: self-assembled monolayer.

less critical with silanes on silica surface. The cleavage of the gold sulfur bond and the desorption of the thiols occurs at around 60 °C in liquid, and begins at 170 °C in ultra high vacuum (UHV), [1,31]. In order to achieve deposition onto well organized, crystalline organic monolayers, the deposition temperature needs to be below the glass transition temperature of the SAM, typically below 120 °C, [31].

Copper deposition has been carried out successfully on 3-mercaptopropyltrimethoxysilane (MPTS) SAMs with Cu(II)bis-hexafluoroacetyl-acetonate, Cu^{+1}(hexafluoroacety1acetonate) tri-methylvinylsilane or (hexafluoroacetyl-acetonato) (vinyltrimethylsilane)copper(I) OMCVD precursors, respectively [32-35].

Palladium and platinum OMCVD was performed with bis(hexafluoroacetylacetonate)platinum(II), bis(hexafluoroacetylacetonato)palladium(II) and cyclopentadienylallylpalladium directly on ITO (indium tin oxide) and SiO_2/Si wavers with a patterned OTS (octadecyltrichlorosilane) SAM as a resists and on 4,4'-biphenyldithiol SAMs self-assembled on silver, [36-40]. Aliganga et al. [41] have used liquid mercury at room temperature without the preparation of an organometallic precursor to deposit nanodroplets onto 1,8-octanedithiol SAMs with the aid of the Hg's vapor pressure.

GaN thin films were grown in solution with the help of the OMCVD precursor $Ga(N_3)_3NEt_3$ in toluene on 11-mercaptoundecanol SAMs. The -OH surface groups of the SAM reacted with the gallium precursor yielding NH and covalent gallium-oxygen bonds, [42].

Very successfully AuNPs have been grown with the help of the OMCVD precursor trimethyl-phosphinegoldmethyl ($(CH_3)_3PAuCH_3$) on dithiol SAMs on Ag and Au and on MPTS SAMs on glass, glass waveguides and oxidized silicon wavers [39, 43-52].

The thermodynamically more labile precursors, as is typical for OMCVD, offer a solution to the problem of coating temperature sensitive surfaces.

The particular interest in OMCVD of Au on top of SAMs in general, was initiated by the aim to depositing ultrathin layers of Au on top of a SAM as a key step in the fabrication of integrated photonic devices designed to act as biosensors. Photonic waveguide devices with high sensitivity, as sensor transducers, are based on glass or silicon materials with oxidic surfaces and are incompatible with extended metal surfaces. These will cause high absorption which lead to unacceptably high waveguide losses, and therefore to only short propagation and interaction lengths. In addition, many suppliers of fine chemicals and biomolecules offer sulfur based compounds and biological recognition pairs, such as antibody-antigenes, with a binding ability to gold and silver, but not necessarily the adequate silane derivative for binding to an oxidic surface.

Recent years, have seen a tremendous impact on AuNP optical response in biological assays, detection, labeling, and sensing, both in theoretical and experimental work, [53-58]. In particular the absorption feature of metal nanoparticles, the localized surface plasmon resonance (LSPR), plays an important role due to its sensitivity to environmental changes of the AuNPs. The LSPR shifts by a few nm to higher wavelength by coating the AuNPs, however when the AuNPs are clustered into aggregates a huge shift of up to 200 nm is observed.

Also many prototype devices in molecular electronics have been proposed or demonstrated, which incorporate AuNPs as components include single electron transistors, single-electron charging devices, photonic switches, and quantum dots, [59-63].

Taking the absorption losses of the optical devices into account and the phenomenal possibilities AuNPs offer in sensing technology, the aim is the deposition of only minute amounts of gold in form of AuNPs on top of a waveguide, functionalized with MPTS. This will then allow creating a sensor platform which can easily be functionalized with the help of the well established SAM sulfur chemistry in the form of thiols, sulfides and disulfides.

Two device platforms were demonstrated with OMCVD grown AuNPs. The first was an optical Mach-Zehnder interferometer, [52]. Here both arms of the silicon oxynitride interferometer were completely functionalized with MPTS and covered by about 10 % with OMCVD AuNPs. The Mach-Zehnder Interferometer was operated outside the LSPR of the AuNPs; the AuNPs served as locations of the bio-recognition SAMs only. Biotin - streptavidin and biotinilated antibody recognition was detected with a sensitivity for streptavidin of 20 ng/cm^2.

A DNA hybridization sensor [64] was build taking advantage of the enhanced evanescent fields the AuNPs show when in LSPR, [65]. Here first AuNPs were grown with a LSPR absorption maximum at 520 nm. After immobilization of biotin and successively streptavidin, a biotinilated catcher DNA half strand was attached to the bio-SAM via the free binding sites for biotin in the straptavidin layer. The target DNA carried a Cy3 dye which absorbs at ~540 nm and emits Stoke shifted at ~ 570

nm. The hybridization reaction with no mismatch and with one base pair mismatch could easily be followed by monitoring the fluorescence emission of the label. The adsorption and desorption kinetics could be fitted to a Langmuir model and a difference in the binding constant between the two hybridization reactions (no mismatch and one mismatch) of more than two orders of magnitude was found.

1.2 OMCVD OF CU ONTO PATTERNED MPTS SAMS AND ON OTS AS A BLOCKING RESIST

Liu et al. [32] have used MPTS SAMs on silicon substrates. They have chemically treated the MPTS SAM to form disulfide or sulfonic terminal groups. They deposited Cu-grains, and closed Cu-films with Cu(II)bis-hexafluoroacetylacetonate at 80°C. Various substrate temperatures, from 270°C to 310°C and substrates with the three terminal groups, -SH, -SS- and SO_3H, were used. The authors found that the –SS–terminal group surface reduced Cu-deposition and the $–SO_3H$ terminal group surface enhanced copper deposition in comparison with the –SH terminal group. An interesting application of this selectivity is a patterned CVD Cu film deposition. A SO_3H/OH pattern as a SAM template was created by UV-light irradiation through a mask for 30 min. at 185 nm on an SO_3H terminated SAM. The mask was in the form of a Z with a line of 0.65 mm width. The sample after OMCVD Cu-growth looked redish with an empty Z in it. Electron microscopy confirmed the non-irradiated area carried a closed Cu-film, whereas the radiated area only carried a few Cu-particles.
Jeon et al. [36] had stamped OTS onto Al/Al_2O_3 and on Si/SiO_2 as a Cu-growth blocking resist. Indeed, by applying (hexafluoroacetylacetonato) (vinyltrimethylsilane)copper(I) Cu-pattern on the surface could be fabricated.

1.3 OMCVD OF PD AND PT ONTO PATTEREND OTS SAMS AS A BLOCKING RESIST

Jeon et al. [37,38] have used OTS SAMs and the OMCVD precursors bis(hexafluoroacetyl-acetonato) platinum(II), and bis(hexafluoroacetyl-acetonato) palladium(II) on titanium nitride (TiN), indium tin oxide (ITO), SiO_2/Si, sapphire, and borosilicate glass. They had chosen substrate temperatures of 175- 275 °C for Pd and 200-350 °C for Pt. The authors were able to grow thin films of platinum and palladium in-between the stamped OTS SAMs onto the directly uncovered substrates with a lateral resolution of the finest line of 1.5 µm. Platinum films deposited above 325 °C consist of round grains with smooth surfaces, in sharp contrast to the faceted, rough surfaces seen below 325 °C. This phenomenon was universal in that identical results were observed for different substrates.

1.4 OMCVD GROWN AU ON STAMPED SAMS ON AU/MICA

To investigate the selectivity of the Au-OMCVD, patterned SAMs were applied. Using the technique of microcontact printing [38], substrates were fabricated exhibiting a µm scale grid of growth and non-growth organic SAM surfaces. Figure 1a shows an AFM image of the first step in the preparation of the lateral structured SAM. A pattern of 1-hexadecanethiol (HDT) was transferred via a PDMS stamp onto a gold-coated mica substrate. The 40 µm x 40 µm squares on the substrate, to which the adsorbates are transferred, are about 16 nm in height. Between the HDT-SAM areas, uncoated regions remained. These regions were filled with a 1,8-octanedithiol (OCDT) SAM by immersion of the substrate in a solution of OCDT for 12 h. Figure 1b shows the resulting 2D microstructured SAM composed of HDT areas and OCDT areas. The height difference, measured by AFM, is about 8 nm, which is about half of the initial height difference of the HDT structure relative to the uncoated regions of the substrate. The patterned structure now exhibits elevated H_3C-terminated non-growth surfaces, and lower HS-terminated growth surfaces. OMCVD of Au was performed. The AFM image (Fig.1c) shows an inversion of the relative heights of the respective areas. After sufficiently long Au deposition, the former thiol-terminated growth areas of the OCDT-SAMs are now the elevated regions, and the non-growth methyl-terminated sites of the HDT-SAMs are lower by about 16 nm. Also, these HDT squares of initial dimensions 40 µm x 40 µm had shrunk to 30 µm x 30 µm. This is apparently because of a lateral overgrowth of the Au coating from the OCDT areas onto the HDT areas. Physical gold deposition does not recognize the SAM template, [45].

Figure 1. AFM images of a) HDT SAM stamped on Au/mica, b) filled with OCDT and c) OMCVD grown Au.

1.5 OMCVD GROWN GOLD NPS IN ROWS ON SNOM NANOLITHOGRAPHICALLY MANIPULATED HDT SAMS ON AU

UV irradiation of alkylthiol SAMs on gold or silver in the presence of air results in the photooxidation of the relatively strong alkylthiolate adsorbate complex to yield an alkylsulfonate. The weakness of the SO_3-Au interaction facilitates the displacement of the alkylsulfonate by a different thiol adsorbed from solution [66,67].

Figure 2. Scheme of SNOM patterning an HDT SAM, substituting OCDT and growing AuNPs. a) SNOM writing, b) removing of HDT, c) re-filling with OCDT and OMCVD growth of AuNPs.

With the aid of a SNOM (scanning near field optical, also NSOM) fiber [68,69] operated at a wavelength λ = 244 nm lines of alkylsulfonate were written in a HDT SAM on Au/mica followed by a self-assembly step with OCDT (Fig.2). The now present thiol groups serve as nucleation sites. AuNPs in the SH-terminated lines were then successfully grown with $(CH_3)_3PAuCH_3$ (Fig.3) [70].

Figure 3. AFM image of the AuNP lines on a patterned HDT SAM.

1.6 OMCVD GROWN AUNPS ON CU^- ION PATTRNED OTS SAMS ON OXIDIZED SILICON WAVERS

OTS as a "resist" was self-assembled on oxide surfaces of silicon wavers to protect the surface from general AuNP growth (Fig.4a). The next crucial point to consider is the ability to damage or remove the OTS SAM to selectively generate a destroyed or "empty" silica surface. To selectively grow AuNPs and to analyze the OTS SAM removal process, 1 cm × 1 cm areas of the OTS coated samples were bombarded (or irradiated) with a relatively wide beam of accelerated Cu^- ions. The other areas remained unirradiated, by using a mask for shielding, to check for the consistency of OTS deposition (Fig.4b).
The OTS removed regions are used as is or re-filled with MPTS (Fig.4c). Again the mercapto groups serve as nucleation sites for the OMCVD AuNP growth (Fig.4).

Figure 4. Scheme of patterning OTS SAMs with ion bombardment, re-filling with MPTS and OMCVD growth of AuNPs.

Despite an electron irradiation promoted exchange reaction approach was demonstrated as a platform for the preparation of mixed SAMs [71] which is potentially able to be implemented in lithography and patterning of SAMs, the alternative route with ion bombardment was followed. Ion irradiation damages and removes organosilane SAMs [72], depending on the applied dose. Ion beam dose refers to the number of ions that are impacted and absorbed into a target through a defined area and carries the unit: ions/cm^2, [73]. Since at higher ion doses more OTS SAM can be expelled, more empty surfaces should be available for the MPTS refill-self-assembly which should directly lead to an increased number of OMCVD AuNPs. The OTS SAM removal process with respect to the different ion doses was studied by contact angle measurements, survey and high-resolution X-ray photoelectron spectroscopy (XPS). In order to quantitatively measure the amount of OMCVD Au NPs, Rutherford backscattering spectroscopy (RBS) and high-resolution XPS were carried out. Scanning electron microscopy (SEM) image analysis was performed to statistically obtain the lateral size (diameter) distribution of the randomly grown AuNPs. In addition to the experiments with MPTS re-filling, the formation of AuNP directly after ion irradiation and its dose dependence were studied by SEM and RBS to demonstrate the importance of the MPTS re-filling process.

Figure 5. SEM image of the edge between irradiated (left) and non-irradiated (right) side of sample. Here the sample with the worst contract between the two sides was chosen to show the "worst case scenario".

The distribution of the OMCVD grown Au NPs is random, as shown in the SEM images in Fig.5. This SEM image was taken at the edge between unirradiated and irradiated sides of a sample treated by an ion dose of 2×10^{15} ions/cm^2. The difference between number of AuNPs grown on the unirradiated and the irradiated sides can clearly be seen. However, this particularly chosen SEM image indicated that the unirradiated side of the chosen example can have plenty of "undesired" AuNPs. 356 particles were counted here in an area of ~21 μm^2, while this number was ~100 in the SEM images of the other unirradiated sides. In practice, the samples can show a much higher contrast between

growth and non-growth areas, but there is always some AuNP growth on the unirradiated sides (undesired Au NPs) due to surface inhomogeneities.

Figure 6. Histograms lateral size (diameter) distribution of a) the sample irradiated at 2×10^{15} ions/cm^2 and b) its non-radiated reference side.

The histograms in Fig.6 present the lateral size distribution of the Au NPs on the irradiated and unirradiated sides shown in the SEM images of Fig.5. The two lateral size distributions for the irradiated and unirradiated sides show slightly different averaged diameters, with values of 37 ± 0.5 nm and 32 ± 0.5 nm, respectively. It had been shown previously that a dilution of nucleation sites changes the size distribution, [46]. Commonly, the size of the AuNPs is controlled by the OMCVD time, [45].

Due to the CH_3-terminated head-groups of OTS, an OTS SAM depicts a hydrophobic surface. Contact angles were measured on the ion irradiated and unirradiated side of the samples. Fig.7 shows that the contact angle is constant at ~110^o for all unirradiated sides as expected for hydrocarbon-terminated surfaces. At a dose of 0.1×10^{15} ions/cm^2 the contact angle on the irradiated side drops by ~ 18^o with respect to its unirradiated reference side. This decrease in contact angle continues to ~ 66^o difference at the highest administered dose of 2.0×10^{15} ions/cm^2. The ion irradiation decreases the surface hydrophobicitiy exponentially with increasing ion dose. The OTS SAM resist is systematically damaged and removed.

Figure 7. Contact angle versus dose

Onto this systematically damaged or destroyed surfaces MPTS was re-filled and AuNPs grown under identical conditions. Fig.8 shows SEM images with systematically increasing dose.
The reference side (a) shows only a few AuNPs and with increasing does the amount of AuNPs increases. However, there is an interruption in this trend at the dose (d) 5 x 10^{14} ions/cm^2. This interrupted trend was also seen in XPS (X-ray photoelectron spectroscopy [74]) investigations and Rutherford Back Scattering (RBS) studies, [49].

Figure 8. SEM images of OMCVD grown AuNPs with MPTS re-filling for the sample irradiated at (b) 1.0×10^{14}, (c) 2.5×10^{14}, (d) 5.0×10^{14}, (e) 7.5×10^{14}, and (f) 1.0×10^{15} ions/cm^2; along with the sample (g) irradiated at 2.0×10^{15} ions/cm^2, (a) its non-irradiated reference side.

High-resolution XPS was performed within Au(4f) binding energy peaks. The peak presented as "dose zero" was measured on the unirradiated side of the sample irradiated at 2×10^{15} ions/cm^2. Except for the first two lower doses (1.0 and 2.5 $\times10^{14}$ ions/cm^2) Fig.9 shows the exponential growth of the Au($4f_{5/2}$) and the Au($4f_{7/2}$) peaks.

Figure 9. XPS Au($4f_{5/2}$)- and the Au($4f_{7/2}$)- peaks versus dose.

In order to investigate the dose dependency of OMCVD AuNP growth in the absence of MPTS re-filling and, therefore, in the absence of SH-groups, a series of samples were placed in the OMCVD chamber quickly after the ion irradiation. SEM images (Fig.10a) showed that the non-irradiated sides resisted the gold deposition very well, as expected. In contrast, the SEM images of the irradiated sides show that the OMCVD process was able to deposit AuNPs onto the OTS damaged or removed areas, even without MPTS refilling. However, in the non re-filled areas mainly AuNP aggregates were formed. The reactivity of the OMCVD process in the MPTS-free areas was enhanced and, therefore, less controllable in comparison to the MPTS involving process. Fig.10 shows that the density of the deposited AuNPs increased systematically with increasing ion doses. Except for the very small doses (<2.5×10^{14} ions/cm^2) the AuNPs clustered and almost formed a close packed AuNP layer, instead of well-defined individual particles. Therefore, this one-step simpler method is not able to produce AuNPs with a controlled "average-spacing" necessary for sensor applications.

Figure 10. SEM images of OMCVD grown AuNPs without MPTS re-filling for the sample irradiated at (b) 1.0×10^{14}, (c) 2.5×10^{14}, (d) 5.0×10^{14}, (e) 7.5×10^{14}, and (f) 1.0×10^{15} ions/cm^2; along with the sample (g) irradiated at 2.0×10^{15} ions/cm^2, (a) its reference side.

1.7 OMCVD GROWN AUNPS ON GA$^+$ ION FIB PATTRNED OTS SAMS ON OXIDIZED SILICON WAVERS

Sub-100 nm lateral resolution 30kV Ga^+ bombardment experiments were carried out by a Zeiss LEO 1540 FIB/SEM Microscope at a beam current of 5 pA, [73]. Hereby the OTS SAM is removed or partly destroyed in a defined pattern by a fine beam of Ga^+ ions. Fig.11a shows the design of the pattern. Each set of lines represents a particular dose controlling the amount of OTS removal. The width profiles of the lines in the patterned OTS could be kept almost all the same: at ~80 nm. However, a gradient can be seen from the highest dose (vertical lines) to the lowest dose (horizontal bottom lines) (Fig.11), which is due to the darker inner lines starting to appear at a dose of ~1 nC cm^{-1} in the centre of the designed lines. These inner lines, which are the Si surface itself, become wider with increasing dose, up to the maximum width at a dose of ~7 nC/cm. Re-filled MPTS molecules should ideally be self-assembled into these inner "empty lines silicon surface".

Figure 11. (a) Designed pattern and (b) SEM image of a FIB nano-lithographically patterned OTS SAM on a Si substrate with different sets of doses. Each set contains 10 lines with line separation = 800 nm, horizontal line length = 40 μm, and line width ≈ 80 nm for doses 0.5-10 nC/cm.

Ga^+ ions were expected to target the methyl (-CH_3) and methylene (-CH_2-) groups of OTS and to effectively change the depth profile inside the lines. The thickness of an OTS SAM with fully extended alkyl chains oriented normal to the surface is about 25 Å, [75]. This thickness varies depending on the orientation of the OTS molecules, [76] e.g. 15 Å was reported for a disordered monolayer, [77]. Fig.12 depicts atomic force microscopy (AFM) images of the FIB patterned OTS SAM with relatively low (0.5 nC/cm) and high (15 nC/cm) doses. The depth of the lines was ~1 nm at a dose of 0.5 nC/cm and ~ 3 nm at 15 nC/cm, respectively. FIB was therefore able to completely remove the OTS SAM in the lines at a dose within 0.5-15 nC/cm.

A threshold can be defined with this dose, at which the Ga^+ ions reached the silica surface, causing a complete (not partial) removal of the OTS SAM. After refilling the lines with MPTS, it was expected to find an increasing amount of MPTS molecules bound into the lines and consequently a larger number of Au NPs grown onto the thiols, up to the threshold dose and then followed by a plateau.

Figure 12. AFM images of OTS FIB nano-lithographically patterned lines at a dose of (a) 0.5 nC /cm and (b) 15 nC/cm.

In order to characterize the OTS SAM removal process, ToF-SIMS (time-of-flight secondary ion mass spectrometry) [78] technique was implemented. Although ToF-SIMS has been applied to relatively small surface areas, it was technically impossible to study the surface chemistry inside a sub-100 nm wide line. Therefore, the averages of ion intensities detected from sets of 10 lines, which together correspond to a FIB dose, were analyzed. This yielded a large enough area to receive distinguishable ToF-SIMS ion intensities, but averaged with unbombarded surface areas. H^-, O^-, OH^-, CH^-, and SiO_2^- ion intensities showed a contrast between FIB bombarded and unbombarded areas. The changes in the ion intensities with respect to the FIB doses were calculate and are depicted in Fig.13.

Figure 13. Normalized ToF-SIMS ion intensity difference of H^-(♦), O^-(■), CH^-(●), and SiO_2^-(▲) versus Ga^+ ion dose of FIB nano-lithographically patterned OTS SAM on a Si substrate. The solid, dash, dot, and dash-dot lines represent Boltzmann fitting curves to CH^-, H^-, O^-, and SiO_2^- ion intensity difference data, respectively.

Because the OTS molecules mainly consist of carbon, the high ratios containing carbon suggest a high OTS content. The strongest ToF-SIMS signal received from the ions including carbon was the CH^- ion. As shown in Fig.13, the average ion intensity of the CH^- ion decreases with increasing FIB dose and start to remain constant after ~7 nC/cm, which is defined as the "threshold" dose. The ion intensity for hydrogen, existing in the alkyl chains, indicated almost the same trend; as it decreases until ~7 nC/cm then continues as plateau. The changes of these two ion intensities confirm the OTS SAM removal, i.e. partly removal up to, and then a complete removal after the threshold dose. In contrast to the H^- and CH^- ions, the O^- and SiO_2^- ion intensities increased with increasing FIB doses up to the threshold, being due to an increase in the OTS SAM removal, and therefore, more signal from the empty silica surface inside the lines could be detected. In the light of the overall results from AFM and ToF-SIMS, it was concluded that focused beam of Ga^+ ions could effectively remove of the OTS SAM with a control on the removal rate by varying the dose, and a threshold dose could be defined about 7 nC/cm.

Figure 14. SEM images of FIB nano-lithographically aligned OMCVD Au NPs with diameters of ~10 nm, after performing MPTS refilling; at a dose of (a) 2 nC/cm, (b) 4 nC/cm, and (c) 10 nC/cm.

The last step before Au OMCVD process is the re-filling of the empty lines with the SH-terminated silane MPTS. SEM images in Fig.14 shows the AuNPs grown in the lines at the end of the entire process. It shows a selective AuNP growth in the FIB nano-lithographically patterned lines with a dose-dependent control on density. A general increase in the number of AuNPs grown in the lines with increasing FIB doses is visual. A decrease in the distances between neighboring Au NPs is the result.

Figure 15. Average center-to-center spacing (along with the standard error as an error bar) between neighbouring NPs in the lines versus Ga^+ ion dose for the OMCVD grown Au NPs (a) after performing MPTS refilling with an exponential decay fit and (b) without performing MPTS refilling with a horizontal linear fit.

To calculate the average-spacing, the nearest neighbor distances (NNDs) of AuNPs (center position of each particle) along the lines were measured. The average spacing versus the FIB dose is plotted in Fig.15 together with an exponentially decaying fit to the data. At the minimum dose (0.5 nC/cm) only 2-3 AuNPs in the ~5.5 µm long lines with an average-spacing of ~2 µm was found. This spacing behavior decreases to 0.3 µm at 5 nC/cm. While the average spacing difference between the 0.5 and 5 nC/cm doses was ~1.8 µm, this difference was only ~100 nm between the 5 and 10 nC/cm doses. In addition, the average-spacing corresponding to the 7 nC/cm dose on the fitting curve was 220 nm, only ~20 nm difference from the 10 nC/cm dose. Therefore, the threshold dose found from the ToF-SIMS results is confirmed at ~7 nC/cm by the AuNP growth process, and the average-spacing does not change significantly after this dose.

Figure 16. SEM images of FIB nano-lithographically aligned OMCVD Au NPs with diameters of ~20 nm, without performing MPTS refilling; at a dose of (a) 2 nC cm^{-1}, (b) 4 nC cm^{-1}, and (c) 10 nC cm^{-1}.

The other option to grow AuNPs into the FIB lines is to eliminate the MPTS re-filling process. SEM images in Fig.16 show that in the absence of SH-groups, the growth of the OMCVD AuNPs was increased in density and in size. Here, the average-spacing was minimized to ~57 nm in average. However, the average-spacing differences between the 0.5 and 5 nC/cm doses and the 0.5 and 10 nC/cm doses were only 0.24 nm and 1.66 nm, which were within the calculated uncertainties. Fig.16 confirms that aside from the maximized Au OMCVD, the average-spacing of AuNPs in the lines is not sensitive to the applied FIB dose, as shown in Fig.15.

Both SEM images (Fig.14 and 16) show that the width of the FIB written lines of ~ 80 nm is still too large to align 30-40 nm diameter nanoparticles in "perfect" manner. Smaller FIB writing speeds will enhance the resolution of the FIB process, namely write narrower lines, but at the same time will enhance the writing time and therefore decrease the efficiency and enhance the costs of the process.

1.8 OMCVD GROWN AUNPS ON GA^+ ION FIB PATTRNED OTS SAMS ON OXIDIZED SILICON WAVERS WITH ADDITIONAL DENSITY CONTROL DUE TO THE APPLICATION OF A BINARY MIXED RE-FILLED SAM

The re-filled MPTS molecules can ideally only bind to FIB irradiated lines as demonstrated by the threshold dose. In addition, it was expected that by diluting the solution providing the thiols, the nucleation sites density for AuNP OMCVD growth are reduced [46], and therefore, the number of AuNPs grown in the re-filled lines decreases. This will result in an increase in the average spacing between AuNPs.

Figure 17. SEM images of FIB nanolithography aligned Au NPs at a dose of 0.5 nC/cm (below threshold) refilled with (a) 20 *v/v*%, (b) 40 *v/v*%, (c) 60 *v/v*%, (d) 80 *v/v*%, (e) 100 *v/v*% of MPTS, and (f) without any refilling.

Fig.17 shows the AuNPs formed on the re-filled SAMs in the lines irradiated at the doses of 0.5 nC/cm, below the threshold dose and Fig.18 at a dose of 11 nC/cm, above threshold. Each line in the SEM images corresponds to a solution volume% of re-filled MPTS. It can clearly be seen that the density of the AuNPs increased by re-filling the lines with increasing ratios of MPTS. However, without re-filling the AuNP density was the highest. The lateral sizes of AuNPs were constant at diameters of ~24 nm.

Figure 18. SEM images of FIB nanolithography aligned Au NPs at a dose of 11 nC/cm (above threshold) refilled with (a) 20 *v/v*%, (b) 40 *v/v*%, (c) 60

v/v%, (d) 80 *v/v*%, (e) 100 *v/v*% of MPTS, and (f) without any refilling.

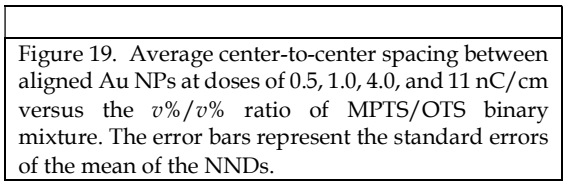

Figure 19. Average center-to-center spacing between aligned Au NPs at doses of 0.5, 1.0, 4.0, and 11 nC/cm versus the *v*%/*v*% ratio of MPTS/OTS binary mixture. The error bars represent the standard errors of the mean of the NNDs.

The NNDs were measured. Although all the 16 doses applied yielded a general decrease in NND with increasing MPTS *v/v*% ratio, four doses (0.5, 1.0, 4.0, and 11 nC/cm) were selected for Fig.19. Almost the same slope of decrease (if linear fitting was applied) was observed for doses higher than the threshold. The difference between minimum and maximum average-spacing of AuNPs grown onto 20 and 100 *v/v*% of refilling MPTS was 106, 96, 49, and 23 nm for doses 0.5, 1.0, 4.0, and 11 nC/cm, respectively.

At doses below the threshold (< ~7 nC/cm), the density of AuNPs is more sensitive to the re-filled binary mixture: the slopes are steeper. However, with increasing doses the slopes decrease systematically. By applying a dose higher than threshold (> ~7 nC/cm), the availability to bind the re-filling SAMs will not change because the incoming refilling molecules bond to completely empty silica surfaces. Therefore, partially removed OTS SAMs remained in the lines after FIB irradiation can improve the control of density and average-spacing between AuNPs and varying the *v/v*% ratios.

1.9 OMCVD GROWN AUNPS ON GA⁺ ION FIB PATTRNED OTS SAMS ON SIO2/ITO/GLASS AND DIRECTLY ON GLASS

In order to create transparent substrates with AuNPs on top which are accessible for spectroscopy, FIB technology was applied to glass samples. In order to create a conductive sample to avoid charge build up during the FIB process in the electron microscope, a thin layer of ITO was deposited on the glass samples (BG11, Schott Grünenplan, Germany). A 140 Å thick layer of SiO_2 was deposited on top of the ITO to allow silane chemistry.

FIB nanolithography performed at lower beam currents (e.g. I=5 pA) leads to narrower lines with sharper edges (see above). However, to pattern the effective ~ 4 mm² area of the UV-Vis light beam in a typical absorption spectrometer, a higher FIB current (I=50 pA) was applied, due to the fabrication time and cost issue. SEM images in Fig.21 show the aligned OMCVD AuNPs grown on SiO_2/ITO/glass substrates. In comparison with uniform OTS SAMs on intrinsic silica surfaces, the SiO_2 layers deposited on top of the ITO layers were not able to form a perfectly protecting OTS SAM against Au NP growth, as seen on the areas outside the lines (Fig.14 and16).

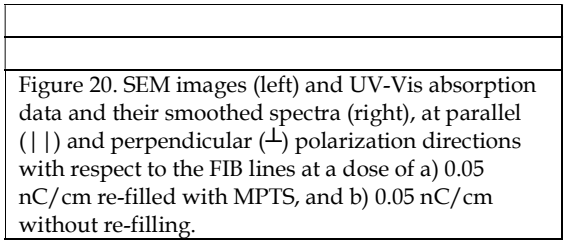

Figure 20. SEM images (left) and UV-Vis absorption data and their smoothed spectra (right), at parallel (||) and perpendicular (⊥) polarization directions with respect to the FIB lines at a dose of a) 0.05 nC/cm re-filled with MPTS, and b) 0.05 nC/cm without re-filling.

The measured average-spacing inside the lines depicted in Fig.20a and b is 38 nm and 39 nm, respectively at an average particle diameter of 25 nm. This is a very small difference. The small difference in the average-spacing is due to the too broad lines written by the FIB process leading to too many grown AuNPs along the entire width of the lines. This fabrication parameter set did not lead to aligned AuNPs. Therefore, the LSPR absorption peak locations (λ_{max}) - either measured with a polarization direction parallel or perpendicular to the lines written with the FIB - do not depend either on the polarization direction or on the applied fabrication parameters.

Aliganga et al. [79] have used BK7 glass (Schott, Mainz, Germany) which was coated directly with OTS without creating a conducting substrate for FIB. A FIB dose of 50 nC/cm was applied. After the FIB process the lines were re-filled with MPTS and AuNPs grown via OMCVD and the $(CH_3)_3PAuCH_3$ precursor. Fig.21 shows aligned AuNPs. However, some difficulties arose in the FIB process and in the imaging process in the SEM due to charging of the substrate, and in absorption spectroscopy due to the minute amount of available AuNPs to take polarization dependent spectra. More work is needed here to optimize the fabrication process.

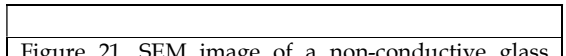

Figure 21. SEM image of a non-conductive glass substrate with aligned AuNPs in FIB written lines.

1.10 CONCLUSION

It was shown in this overview which OMCVD precursors are available for a gentle OMCVD process at mild temperature conditions to allow the brittle SAM structure to survive and foster and

guide the deposition process. Cupper, platinum, palladium, gold, gallium nitride and mercury were demonstrated as deposited thin films or in the form of nanoparticles. SAM patterning had been performed by a simple stamping process involving an inked PDMS stamp to define protected areas and to allow growing metal OMCVD films in the areas without a SAM, the unprotected surfaces. Also, a stamping method has been introduced with a second filling process to define growth and non-growth areas on a closed two-material SAM. In addition, ion bombardment in a large area approach and in a nanolithography approach with a FIB were introduced.

One aim in the AuNP deposition was to achieve a better control on the spacing between neighboring particles, which is an issue in randomly growing objects due to OMCVD and needs to be solved when these particles are supposed to be used in highly sophisticated biosensing application.

It has been shown that ion bombardment indeed can be used to control the density of the nucleation sites, but of cause also only in a statistical fashion. The alignment of OMCVD AuNPs can basically be achieved by FIB nanolithography. However here exists a trade-off between invested FIB writing time and written line width. Therefore the AuNPs have the ability to grow in defined narrow lines in a real alignment within only a few written lines or grow still more or less randomly in wider lines (as long as the written line width is larger than their diameter). The latter allows for absorption spectroscopy in the case of a transparent substrate, but does not yield an anisotropy due to the written stripes, whereas the first suffers in spectroscopy from limited amounts of sample.

1.11 ACKNOWLEGEMENTS

I like to acknowledge all students, postdoctoral fellows and colleagues who have contributed over the years with their work and effort, knowledge and dedication to the deposition of AuNPs on SAMs in general and on patterned SAMs in particular. Here are their names in alphabetical order: Anne Kathrena A. Aliganga, Stefan Busse, Erden Ertorer, Roland A. Fischer, Josua Käshammer, Stephan Krämer, Graham J. Leggett, Touraj Manifar, Laura C. Pavelka, Asad Rezaee, Ulrike Weckenmann, Juri Weiss, Carl Winter, and Peter Wohlfart.

I would also like to acknowledge the institutions involved: The Max-Planck Institute for Polymer Research in Mainz, Germany; The Ruhr-University Bochum, Germany; The University of Sheffield, UK; and the University of Western Ontario in London, Canada.

Financial support came from German and Canadian sources, and their financial contributions are thanked for: Max-Planck Gesellschaft, Deutsche Forschungsgemeinschaft (DFG), the Natural Sciences and Engineering Research Council of Canada (NSERC), the Ontario Centers of Excellence (OCE), the Government of Canada (Canada Research Chair Program), the Ontario Research Development Challenge Fund **(**ORDCF**)** and the Canadian Institute for Photonic Innovation (CIPI).

I also like to thank the Western Nanofabrication Facility and its staff as well as the laboratory of Kim Baines (Department of Chemistry at the University of Western Ontario) for their continuing help.

References

Ulman, A. (1991) *An Introduction to Ultrathin Organic Films* (Academic Press, San Diego, Ca, USA).

Ulman, A. (1996). Formation and Structure of Self-Assembled Monolayers, *Chem. Rev.,* **96**, pp. 1533-1554.

Schreiber, F. (2000). Structure and growth of self-assembled mololayers, *Progress in Surface Science,* **65**, pp.151-256.

Love, J.C., Estroff, L.A., Kriebel, J.K., Nuzzo, R.G., and Whitesides, G.M. (2005). Self-assembled monolayers of thiolate on metals as a form of nanotechnology, *Chem. Rev.,* **105**, pp. 1103-1169.

Terrill, R.H., Tanzer, T.A., and Bohn, P.W. (1998). Structural evolution of hexadecanethiol monolayers on gold during assembly: substrate and concentration dependence of monolayer structure and crystallinity, *Langmuir,* **14**, pp. 845-854.

Miller, M.S., San Juan, R.S., and Carmichael, T.B. (2010), Nanoscale changes to gold

substrate morphology dictate the binding and structure of new dialkyldithiophosphinic acid self-assembled mono-layers, *Nano Letters*, in preparation.

Brust, M., Blass, P. M., and Bard, A. J. (1997). Self-assembly of photoluminescent copper (I) - dithiol multilayer thin films and bulk materials, *Langmuir*, **13**, pp. 5602- 5607.

Deng, W., Yang, L., Fujita, D., Nejoh, H., and Bai, C. (2000). Silver ions adsorbed to self-assembled monolayers of alkanedithiols on gold surfaces form Ag-dithiol-Au multilayer structures *Appl. Phys. A: Mater. Sci. Process.,* **71**, pp. 639-642.

Jiang, W., Zhitenev, N., Bao, Z., Meng, H., Abusch-Magder, D., Tennant, D., and Garfunkel, E. (2005). Structure and bonding issues at the interface between gold and self-assembled conjugated dithiol monolayers, *Langmuir*, **21**, pp. 8751-8757.

Esplandiu, M. J., and Hagenstrom, H. (2002). Functionalized self-assembled monolayers and their influence on silver electrodeposition, *Solid State Ionics,* **150**, pp. 39-52.

Qu, D., and Uosaki, K. (2006). Electrochemical metal deposition on top of an organic monolayer, *J. Phys. Chem. B*, **110**, pp. 17570-17577.

Ohgi, T., Sheng, H.-Y., Dong, Z.-C., Nejoh, H., and Fujita, D. (2001). Charging effects in gold nanoclusters grown on octanedithiol layers, *Appl. Phys. Lett.*, **79**, pp. 2453-2455.

Ohgi, T., Sheng, H.-Y., and Nejoh, H. (1998). Au particle deposition onto self-assembled monolayers of thiol and dithiol molecules, *Appl. Surf. Sci.*, **130**, pp. 919-924.

Boer, B., Frank, M. M., Jiang, W., Garfunkel, E. and Bao, Z. (2004). Metallic contact formation for molecular electronics: interactions between vapor-deposited metals and self-assembled monolayers of conjugated mono- and dithiols, *Langmuir*, **20**, pp. 1539-1542.

Hong Ma, Hin-Lap Yip, Fei Huang, and Alex K.-Y. Jen, (2010). Interface Engineering for Organic Electronics, *Advanced Functional Materials,* 20, pp. 1371–1388.

Usrey, M.L., and Strano, M.S. (2009). Controlling single-walled carbon nanotube surface adsorption with covalent and noncovalent functionalization, *J. Phys. Chem. C,* **113***,* pp. 12443–12453.

Tenboll, A., Darvish, B., Hou, W., Duwez, A.-S., Dixon, S.J., Goldberg, H.A., Grohe, B., and Mittler, S. (2010). Controlled deposition of highly oriented type I collagen mimicking *in vivo* collagen structures, *Langmuir*, in press.

Ista, L.K., Mendez, S., and Lopez, G.P. (2010). Attachment and detachment of bacteria on surfaces with tunable and switchable wettability, *Biofouling*, **26**, pp. 111-118.

Yang, M., and Zhang, Z. (2004). Impediment to heterogeneous electron transfer reactions of redox-active species by alkanedithiol self-assembled monolayers with and without an

adlayer of Au nanoparticles, *Electrochim. Acta,* **49**, pp. 5089-5095.

Bethel, D., Brust, M., Schiffrin, D.J., and Kiely, C. (1996). From monolayers to nanostructured materials: An organic chemist's view of self-assembly, *J. Electroanal. Chem.*, **409**, pp. 137-143.

Stolaczyk, K., and Bilewicz, R. (2006). Electron transport through alkanethiolate films decorated with monolayer protected gold clusters, *Electrochim. Acta,* **51**, pp. 2358-2365.

Chirea, M., Cruz, A., Pereira, C. M., and Silva, A.F. (2009). Size – dependent electrochemical properties of gold nanorods, *J. Phys. Chem. C,* **113**, pp. 13077-13087.

Lu, M., Li, X.H., Yu, B.Z., and Li, H.L. (2002). Electrochemical behavior of Au colloidal electrode through layer-by-layer self-assembly, *J. Colloid and Interface Sci.,* **248**, pp. 376-382.

Su, L., and Mao, L. (2006). Gold nanoparticle / alkanedithiol conductive films self-assembled onto gold electrode: Electrochemistry and electroanalytical application for voltammetric determination of trace amount of catechol, *Talanta*, **70**, pp. 68-74.

Kodas, T., and Hampden-Smith, A. (1994) *The Chemistry of Metal CVD*, (VCH, Weinheim, Germany).

Chopra, N., Bachas, L.G., and Knecht, M.R. (2009). Fabrication and biofunctionalization of carbon-encapsulated Au nanoparticles, *Chem. Mater.*, 21, pp. 1176–1178

Okumura, M., Nakamura, S., Tsubota, S., Nakamura, T., Azuma, M., and Haruta, M. (1998). Chemical vapor deposition of gold on Al_2O_3, SiO_2, and TiO_2 for the oxidation of CO and of H_2, Catalysis Letters, **51**, pp. 53-58.

Barreca, D., Gasparotto, A., Maccato, C., and Tondello, E. (2008). Silica-sandwiched Au nanoparticle arrays by a soft PE-CVD/RF sputtering approach, *Nanotechnology*, **19**, 255602 (8pp).

Palgrave, R.G., and Parkin, I.V. (2007). Aerosol assisted chemical vapor deposition of gold and nanocomposite thin films from hydrogen tetrachloroaurate(III), *Chem. Mater.*, 19*,* pp. 4639-4647.

Araki, H., Fukuoka, A., Sakamoto, Y., Inagaki, S., Sugimoto, N., Fukushima, Y., and Ichikawa, M. (2003). Template synthesis and characterization of gold nano-wires and -particles in mesoporous channels of FSM-16, *Journal of Molecular Catalysis A: Chemical*, **199**, pp. 95–102.

Nuzzo, R.G., Fusco, F.A., and Allara, D.L. (1987). Spontaneously organized molecular assemblies. 3. Preparation and properties of solution adsorbed monolayers of organic disulfides on gold surfaces J. Am. Chem. Soc., **109**, pp. 2358-2368.

Liu, X., Wang, Q., and Wu S., (2006).Characterization of chemical vapor deposited copper films on mercaptan self -

assembled monolayer diffusion barriers, *Chem. Vap. Deposition*, **12**, pp. 679–684.

Papadimitropoulos, G., Arapoyianni, A., and Davazoglou, D., (2008). Hot-wire CVD of copper films
on self-assembled-monolayers of MPTMS, *Phys. Stat. Sol. (a)*, **205**, pp. 2607–2610.

Liu, X., Wang, Q., and Chen, L.-P. (2009). In situ functionalized self-assembled monolayer surfaces for selective chemical vapor deposition of copper, *Applied Surface Science,* **255** (2009) pp. 3789–3794.

Jeon, N.L., Nuzzo, R.G., Xia,Y., Mrksich, M., and Whitesides, G.M. (1995). Patterned self-assembled monolayers formed by microcontact printing direct selective metalization by chemical vapor deposition on planar and nonplanar substrates, *Langmuir*, **21**, pp. 3024-3026.

Jeon, N.L., Lin, W., Erhardt, M.K., Girolami, G.S., and Nuzzo, R.G. (1997). Selective chemical vapor deposition of platinum and palladium directed by monolayers patterned using microcontact printing, *Langmuir*, **13**, pp. 3833-3838.

Jeon, N.L., Finnie, K., Branshaw, K., and Nuzzo, R. (1997). Structure and stability of patterned self-assembled films of octadecyltrichlorosilane formed by contact printing, *Langmuir*, **13**, pp. 3382-3391.

Fischer, R.A., Weckenmann, U., Winter, C., Käshammer, J., Scheumann, V., and Mittler, S. (2001). Area selective OMCVD of gold and palladium on self-assembled organic monolayers: Control of nucleation sites, *Journal de Physique IV*, **11**, pp. 1183-1190.

Weckenmann, U., Aliganga, A.K.A., Mittler, S., Krämer, S., Fischer, R.A. (2004). A Study on the selective organometallic vapor deposition of palladium onto self-assembled monolayers of 4,4′- biphenyldithiol, 4-biphenylthiol, and 11-mercapto- undecanol on polycrystalline silver, *Chemistry of Materials*, **16**, pp. 621-628.

Aliganga, A.K.A., Wang, Z., and Mittler, S. (2004). Chemical vapor deposition of mercury on alkanedithiolate self-assembled monolayers, *J. Phys. Chem. B*, **108**, pp. 10949-10954.

Winter, C., Käshammer, J., Mittler-Neher, S., and Fischer, R. (1998). A new pathway to GaN: Deposition of GaN-clusters on functionalized thiol-SAMs on gold, *Optical Materials*, **9**, pp. 352-355.

Käshammer, J., Wohlfart, P., Weiß, J., Winter, C., Fischer, R., and Mittler-Neher, S. (1998). Selective gold deposition via CVD onto self-assembled organic monolayers, *Optical Materials*, **9**, pp. 406-410.

Wohlfart, P., Weiß, J., Käshammer, J., Winter, C., Scheumann, V., Fischer, R., and Mittler-Neher, S. (1999). Selective ultrathin gold deposition by organometallic chemical vapor deposition onto organic self-assembled monolayers (SAMs), *Thin Solid Films*, **340**, pp. 274-279.

Winter, C., Weckenmann, U., Fischer, R.A., Käshammer, J., Scheumann, V., and Mittler,

S. (2000). Selective nucleation and area selective OMCVD of gold on patterend self-assembled organic monolayers studied by AFM and XPS: a comparison of OMCVD and PVD, *Advanced Materials: CVD*, **6**, pp. 199-205.

Aliganga, A.K.A., Duwez, A.-S., Mittler, S. (2006). Binary mixtures of SAMs of 1,8-octanedithiol and 1-octanethiol for a controlled growth of gold nanoparticles, *Organic Electronics*, **7**, pp. 337-350.

Aliganga, A.K.A., Lieberwirth, I., Glasser, G., Duwez, A.-S., Sun, Y., and Mittler, S. (2007). Fabrication of equally oriented pancake shaped gold nanoparticles by SAM templated OMCVD and their optical response, *Organic Electronics*, **8**, pp. 161- 174.

Rooney, P., Xu, S., Rezaee, A., Manifar, T., Hassanzadeh, A., Podoprygorina, G., Böhmer, V., Rangan, C., and Mittler, S. (2008). Control of surface plasmon resonances in dielectrically-coated proximate gold nanoparticles immobilized on a substrate, *Phys. Rev. B*, **77**, 235446 (9pp).

Rezaee, A., Aliganga, A.K.A., and Mittler, S. (2009). Control of density of randomly grown OMCVD gold nanoparticles by means of ion irradiation, *Journal of Physical Chemistry C*, **113**, pp. 15824-15833.

Rezaee, A., Aliganga, A.K.A., Pavelka, L.C., and Mittler, S. (2010). Control of the average spacing between aligned gold nanoparticles by varying the FIB dose, *Physical Chemistry Chemical Physics*, **12**, pp. 4104 – 4111.

Rezaee, A., Pavelka, L.C., and Mittler, S. (2009). Binary mixtures of SH- and CH_3-terminated self-assembled monolayers to control the average spacing between aligned gold nanoparticles, *Nanoscale Research Letters*, **4**, pp. 1319-1323.

Busse, S., Käshammer, J., Krämer, S., and Mittler-Neher, S. (1999). Gold and thiol surface functionalized integrated optical Mach-Zehnder interferometer for sensing purposes, *Sensors and Actuators B*, **60**, pp. 148-154.

Ambjörnsson, T., Mukhopadhyay, G., Apell, S. P., and Kall, M. (2006). Resonant coupling between localized plasmons and anisotropic molecular coatings in ellipsoidal metal nanoparticles, *Phys. Rev. B*, **73**, 085412 (10pp).

Aslan, K., Zhang, J., Lakowicz, J.R., Geddes, C.D. (2004). Saccharide sensing using gold and silver nanoparticles - A review**,** *J. Fluoresc.*, **14**, pp. 391-400.

Haes, A.J., Stuart, D.A., Nie, S.M., Van Duyne, R.P. (2004). Using Solution-Phase Nanoparticles, Surface-Confined Nanoparticle Arrays and Single Nanoparticles as Biological Sensing Platforms, *J. Fluoresc.*, **14**, 355-367.

Haes, A.J., Zou, S., Schatz, G.C., and Van Duyne, R.P. (2004). Nanoscale Optical Biosensor: Short Range Distance Dependence

of the Localized Surface Plasmon Resonance of Noble Metal Nanoparticles, *J. Phys. Chem. B,* 108, pp. 6961-6968

Mirkin, C. A.; Letsinger, R. L.; Mucic, R. C.; Storhoff, J. J. (1996). A DNA-based method for rationally assembling nanoparticles into macroscopic materials, *Nature,* , *382*, pp. 607-609.

Hashemi Rafsanjani, S.M., Cheng, T., Mittler, S., and Rangan, C. (2010). Theoretical proposal for a biosensing approach based on a linear array of immobilized gold nanoparticles, *Journal of Applied Physics*, **107,** 094303 (6pp).

Klein, D. L., Roth, R., Lim, A.K.L., Alivisatos, A.P.; and McEuen, P.L. (1997). A single-electron transistor made from a cadmium selenide nanocrystal, *Nature,* **389**, pp. 699-701.

Sato, T., Ahmed, H., Brown, D., and Johnson, B.F.G. (1997). Single electron transistor using a molecularly linked gold colloidal particle chain. *J. Appl. Phys.*, **82**, pp. 696-701.

Katz, E., Lioubashevski, O., and Willner, I. (2006). Magneto-switchable single-electron charging of Au-nanoparticles using hydrophobic magnetic nanoparticles, *Chem. Commun.* **2006**, pp. 1109-1111.

De, S., Pal, A., and Pal, T. (2000). Molecular photonic switches employing ions and nanoparticles of coinage and platinum metals, *Langmuir,* **16**, pp. 6855-6861.

Baum, T., Bethell, D., Brust, M., and Schiffrin, D.J. (1999). Electrochemical charge injection into immobilized nanosized gold particle ensembles: Potential modulated transmission and reflectance spectroscopy *Langmuir,* **15**, pp. 866-871.

Aliganga, A.K.A., Xu, F., Knoll, W., and Mittler, S. (2005). Immobilized gold nanoparticles fabricated by template assisted organo metallic chemical vapor deposition for oligonucleotide hybridisaton studies, *SPIE*, **5969**, 0H-1 - 0H-12.

Jensen, T., Kelly, L., Lazarides, A., and Schatz, G.C. (1999). Electrodynamics of Noble Metal Nanoparticles and Nanoparticle Clusters, *Journal of Cluster Science,* **10***,* pp. *295-317.*

Tarlov, M.J., Burgess, D.R.F., and Gillen, G. (1993). UV photopatterning of alkylthiolate monolayers self-assmbled on gold and silver, *J. Am. Chem. Soc.*,, **115**, pp. 5305-5306.

Hutt, D.A., and Leggett, G.J. (1996). Influence of adsorbate ordering on rates of UV photooxidation of self-assembled monolayers, *J. Phys. Chem.,* **100**, pp. 6657-6662.

Chong, T.V., Hong, M.H., and Shi, L.P. (2010). Laser precision engineering: from microfabrication to nanoprocessing, Laser & Photon. Rev., 4, pp. 123–143.

Sun, S., Mendes, P., Critchley, K., Diegoli, S., Hanwell, M., Evans, S.D., Leggett, G.J., Preece, J.A., and Richardson, T.H. (2006). Fabrication of gold micro- and nanostructures by photolithographic exposure of thiol-stabilized gold Nnnoparticles, *NANO LETTERS*, **6,** pp. 345-350

Alignaga, A.K.A., Leggett, G.J., and Mittler, S., unpublished data.

Ballav,N., Shaporenko, A., Krakert, S., Terfort, A., and Zharnikov, M. (2007). Tuning the exchange reaction between a self-assembled monolayer and potential substituents by electron irradiation, *J. Phys. Chem. C*, **111**, pp. 7772-7782.

Ada, E. T., Hanley, L., Etchin, S., Melngailis, J., Dressick, W.J., Chen, M.S., and Calvert, J.M. (1995). Ion beam modification and patterning of organosilane self-assembled monolayers, *J. Vac. Sci. Technol. B*, **13**, pp. 2189-2196.

Giannuzzi, L.A., and Stevie, F.A., (Eds.) (2005) Introduction to focused ion beams: instrumentation, theory, techniques, and practice (Springer: New York, NY, USA).

Watts, J.F., and Wolstenholme, J. (2003) *An introduction to surface analysis by XPS and AES* (Wiley: Chichester, West Sussex, GB, New York, NY, USA).

Angst, L.D., and Simmons, G.W. (1991) Moisture absorption characteristics of organolilane self-assembeled monolayers, *Langmuir*, **7**, pp. 2236-2242.

Mirji, S.A. (2006). Octadecyltrichlorosilane adsorption kinetics on Si(100)/SiO_2 surface: contact angle, AFM, FTIR and XPS analysis, *Surf. Interface Anal.*, **38**, pp. 158-165.

Cho, J.H., Lee, D.H., Shin, H.S., Pattanayek, S.K., Ryu, C.Y., and Cho, K. (2004). Exploiting poly(dimethylsiloxane)-modified tips to evaluate frictional behavior by friction force microscopy, *Langmuir*, **20**, pp. 11499-11503.

Rivière, J.C., and Myhra, S. (Eds.) (2009) Handbook of surface and interface analysis : methods for problem-solving (CRC Press: Boca Raton, USA).

Aliganga, A.K.A., and Mittler, S., unpublished data.

Figures

Fig.1

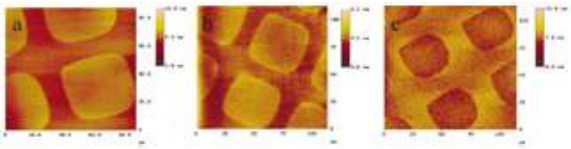

Fig.2

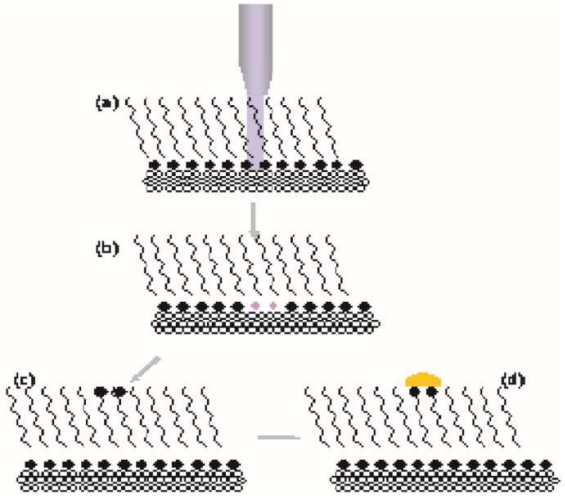

Fig.3

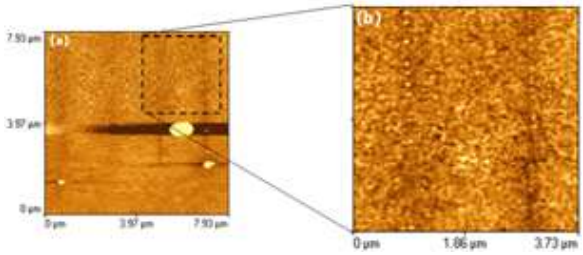

Fig.4

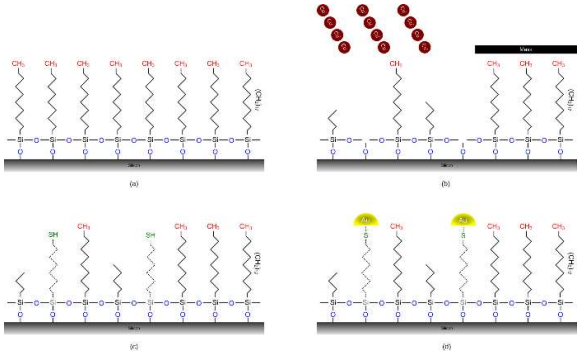

Fig.5

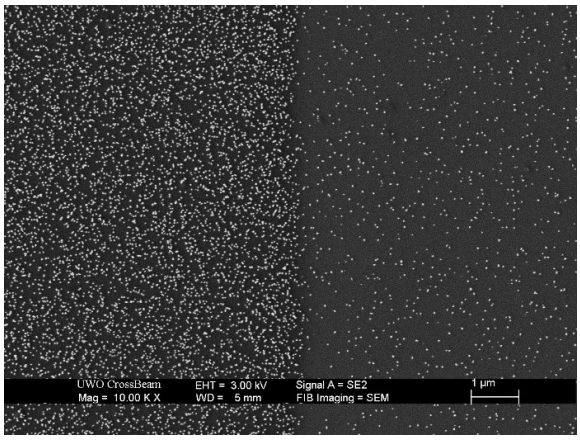

Fig.6a

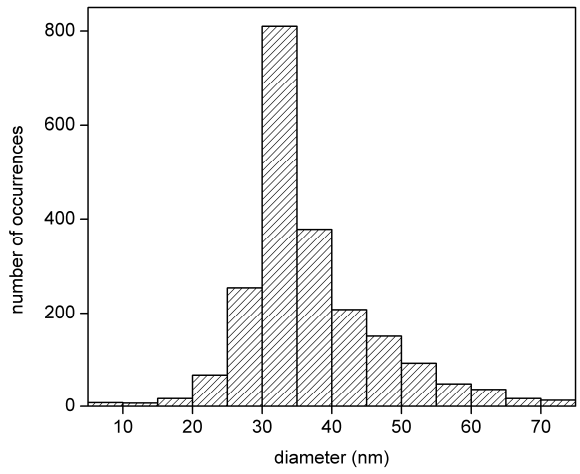

Fig.6b

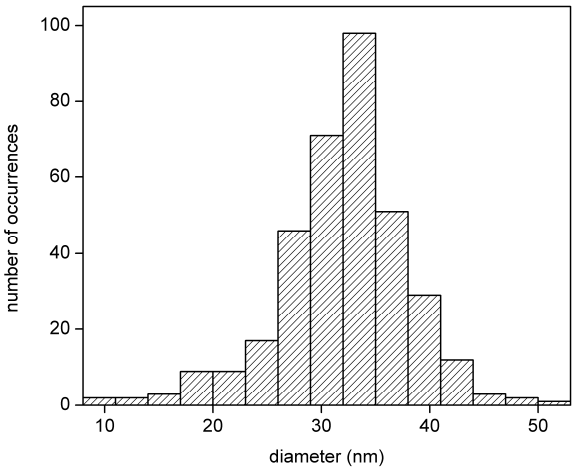
number of occurrences
diameter (nm)
0
20
40
60
80
100
10
20
30
40
50

Fig.7

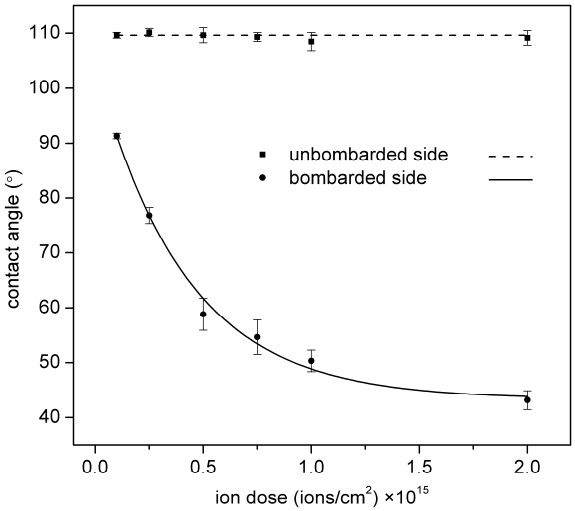
contact angle (°)
ion dose (ions/cm^2) ×10^{15}
unbombarded side
bombarded side
40
50
60
70
80
90
100
110
0.0
0.5
1.0
1.5
2.0

Fig.8

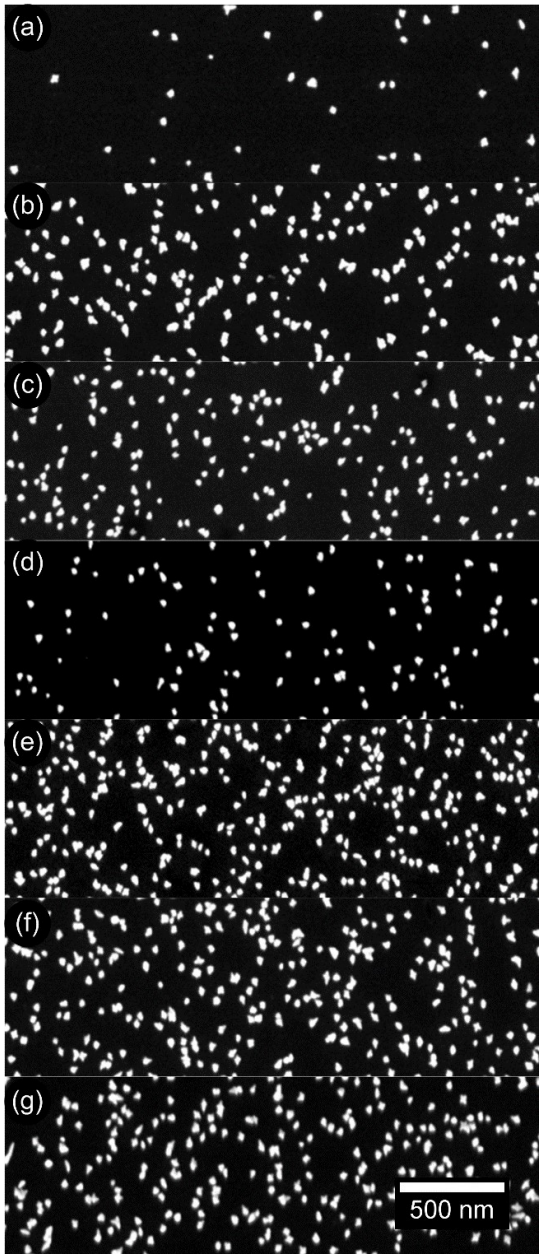
(a)
(b)
(c)
(d)
(e)
(f)
(g)
500 nm

Fig.9

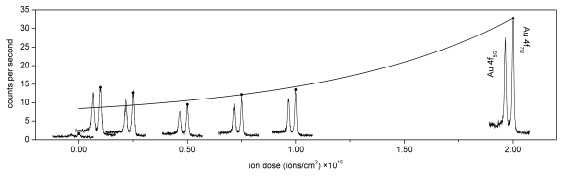
counts per second
ion dose (ions/cm²) ×10¹⁵
Au 4f
Au:4f5/2
Au:4f7/2

Fig.10

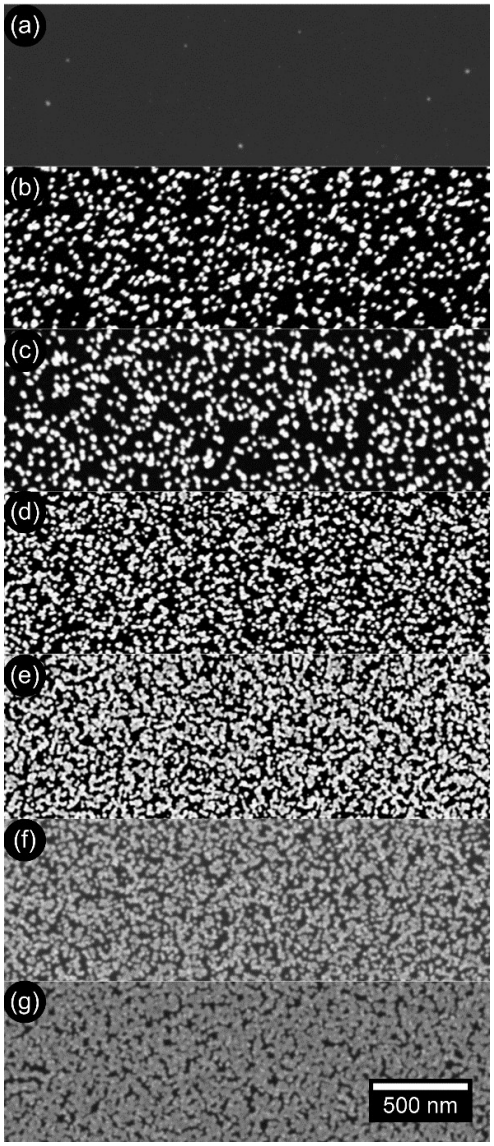

Fig.11

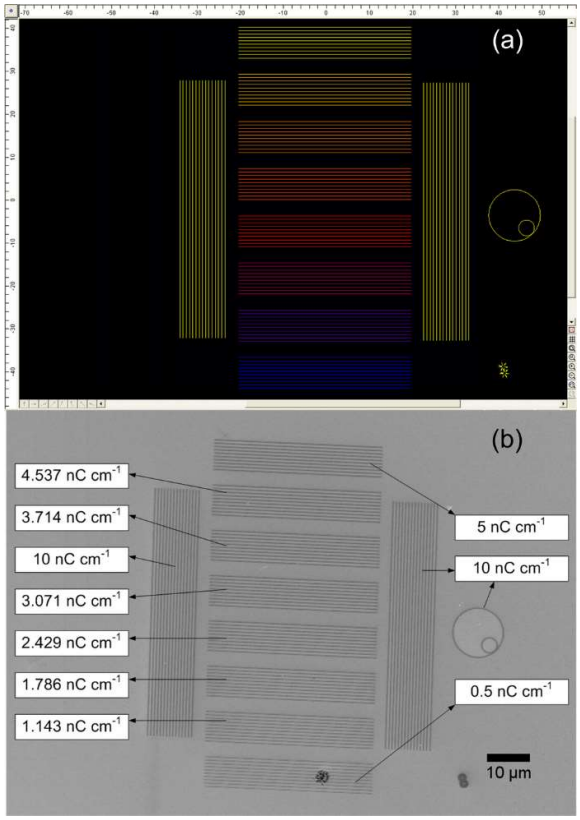
(a)
(b)
4.537 nC cm-1
3.714 nC cm-1
10 nC cm-1
3.071 nC cm-1
2.429 nC cm-1
1.786 nC cm-1
1.143 nC cm-1
5 nC cm-1
10 nC cm-1
0.5 nC cm-1
10 µm

Fig.12

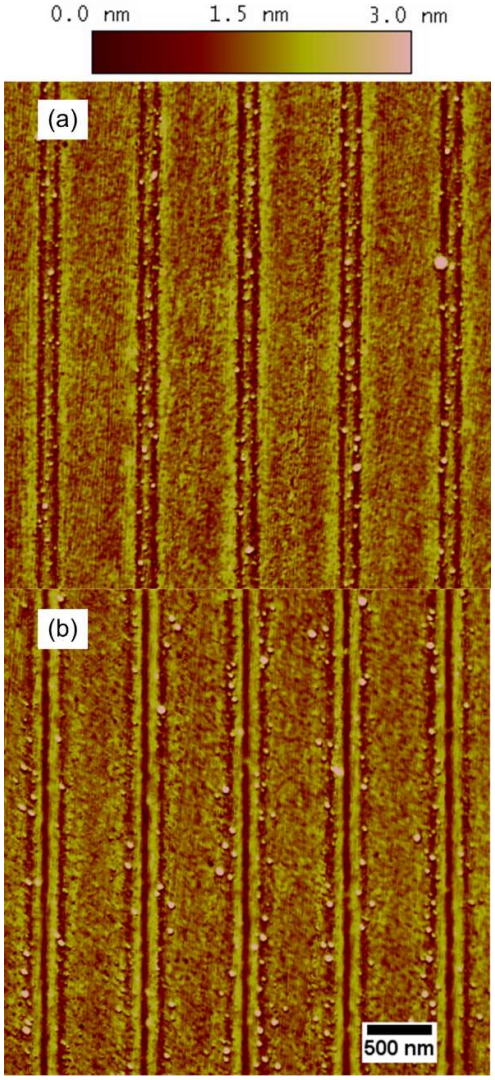

Fig.13

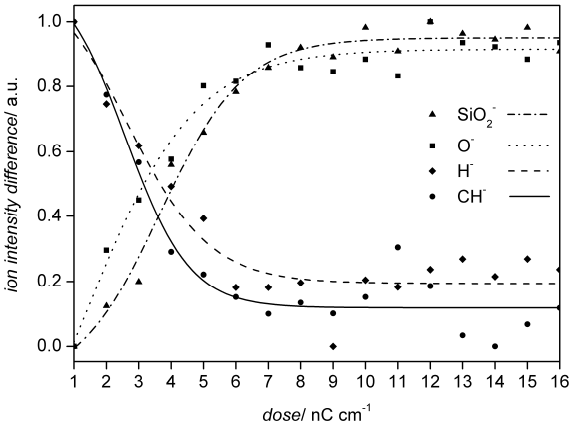
1.0
0.8
0.6
0.4
0.2
0.0
1 2 3 4 5 6 7 8 9 10 11 12 13 14 15 16
ion intensity difference/ a.u.
dose/ nC cm-1
SiO2-
O-
H-
CH-

Fig.14

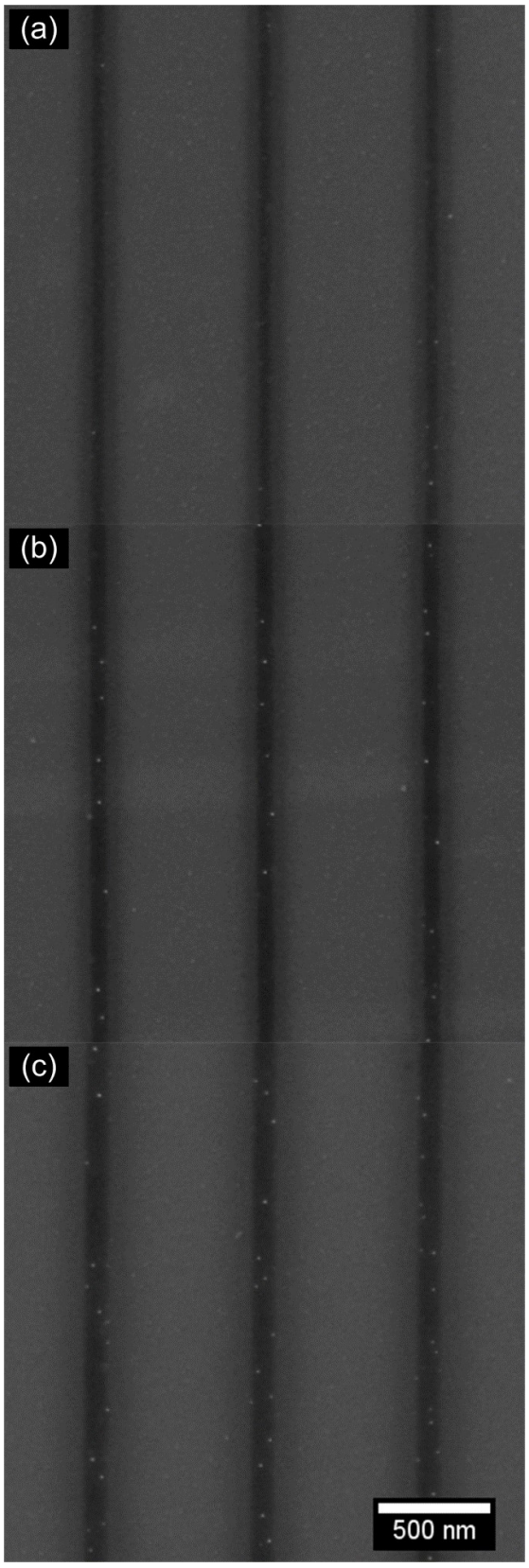

Fig.15

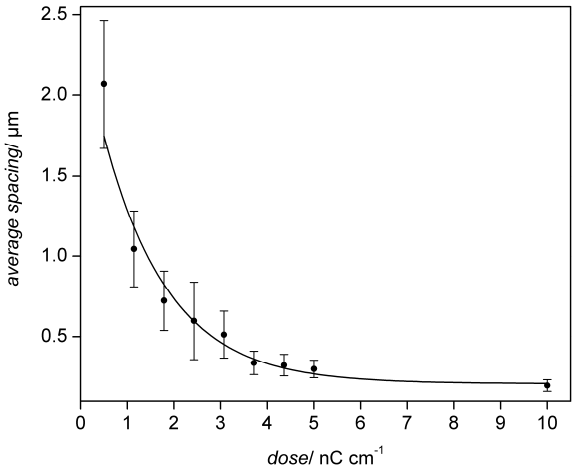

Fig.16

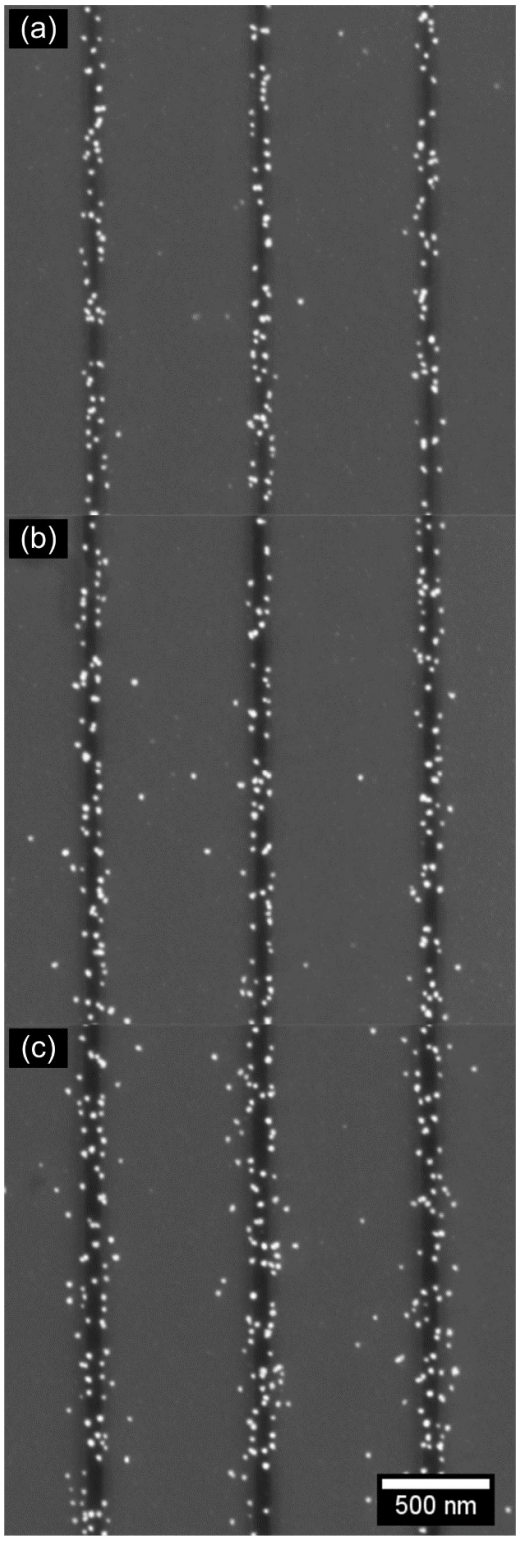

Fig.17

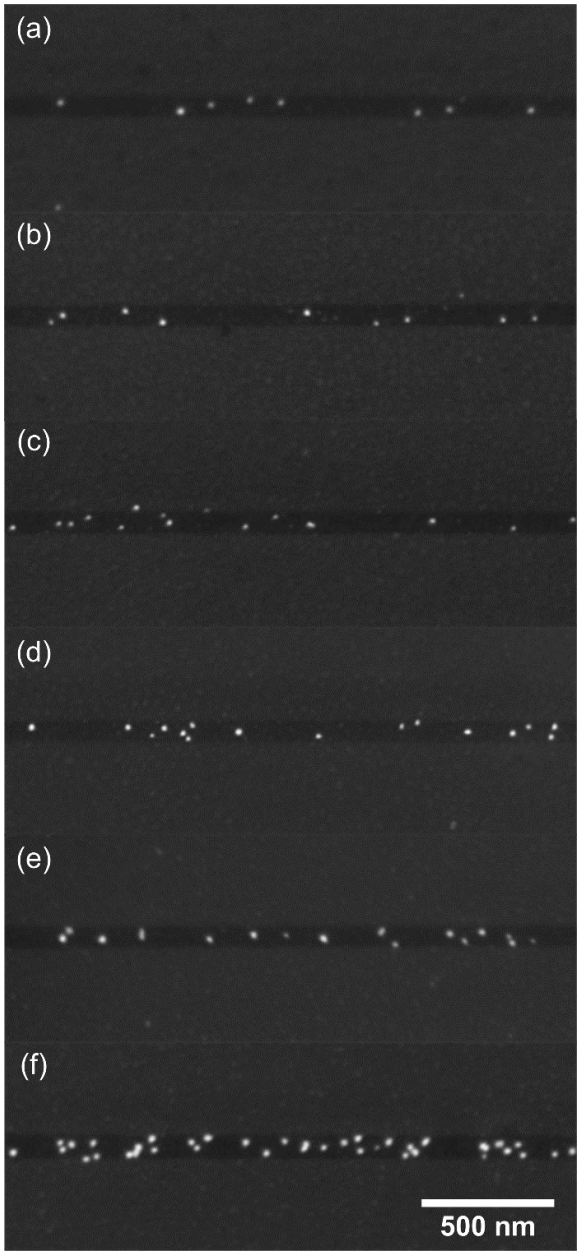

Fig.18

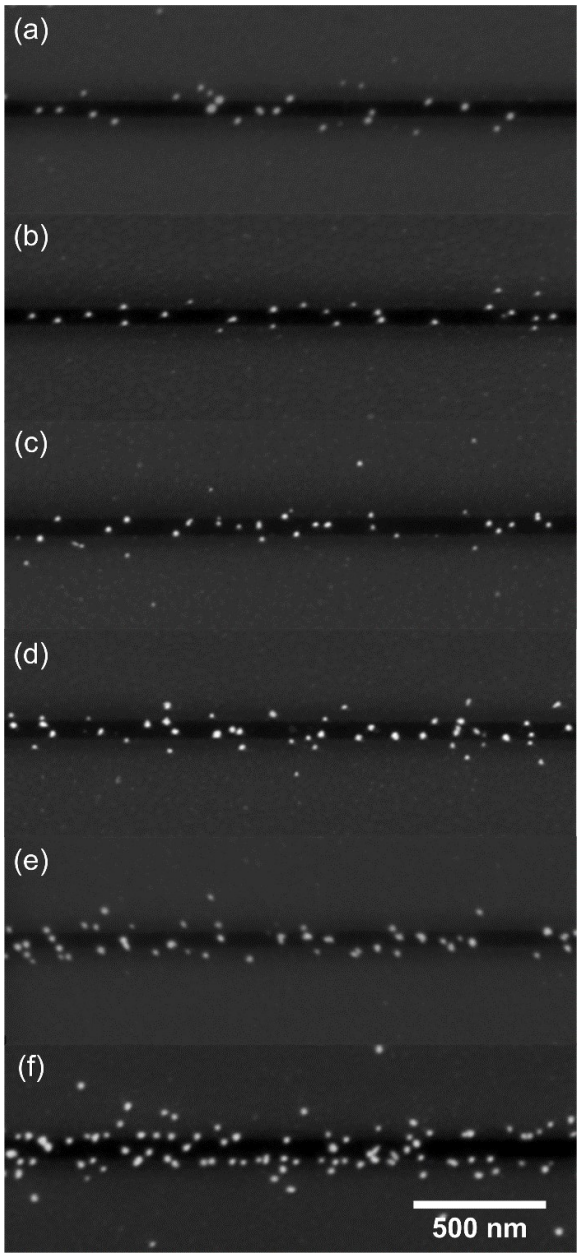

Fig.19

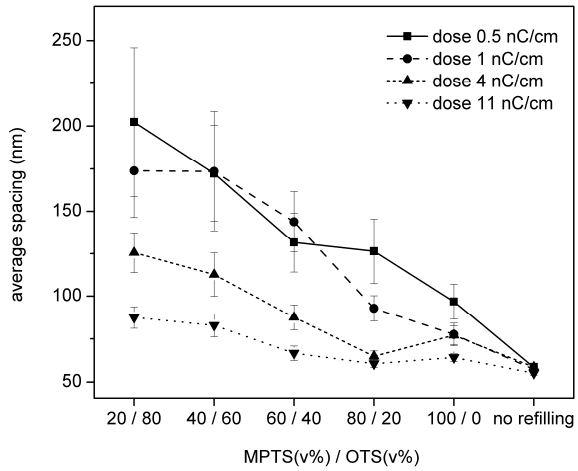

Fig.20a

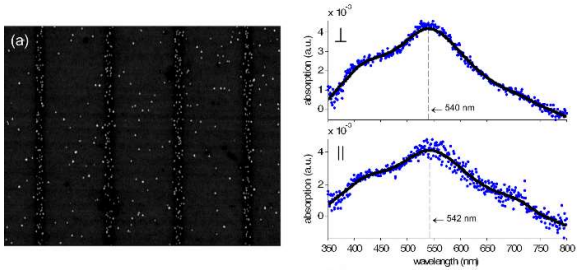

Fig.20b

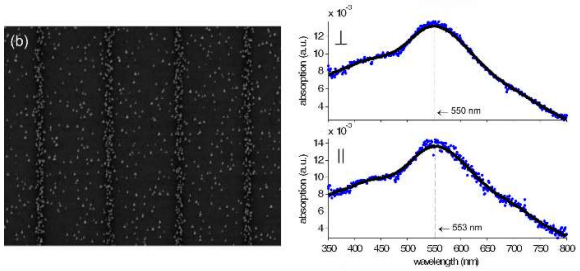

Fig.21

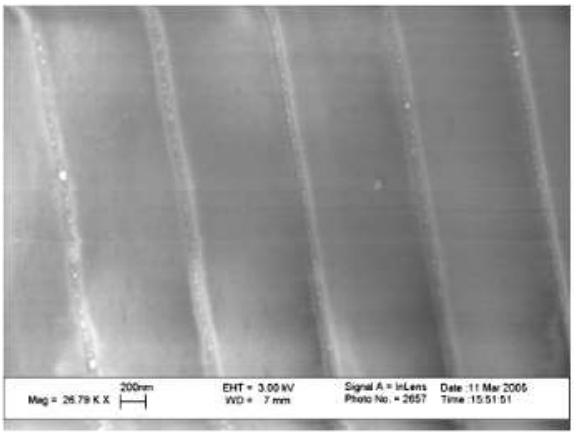
200nm
Mag = 26.79 K X
EHT = 3.00 kV
WD = 7 mm
Signal A = InLens
Photo No. = 2657
Date :11 Mar 2005
Time :15:51:51